

Article

Synthesis and Characterization of B/NaF and Silicon Phthalocyanine-Modified TiO₂ and an Evaluation of Their Photocatalytic Removal of Carbamazepine

Chukwuka B. Anucha ^{1,*}, Ilknur Altin ^{1,*} , Debora Fabbri ² , Ismail Degirmencioglu ¹, Paola Calza ², Giuliana Magnacca ^{2,3} , Vassilis N. Stathopoulos ⁴  and Emin Bacaksiz ¹

¹ Department of Chemistry/Physics, Faculty of Science, Karadeniz Technical University, Trabzon 61080, Turkey; ismail61@ktu.edu.tr (I.D.); eminb@ktu.edu.tr (E.B.)

² Department of Chemistry, University of Turin, Via P. Giuria 5-7, 10125 Turin, Italy; debora.fabbri@unito.it (D.F.); paola.calza@unito.it (P.C.); giuliana.magnacca@unito.it (G.M.)

³ NIS Interdepartmental Centre, University of Turin, Via P. Giuria 5-7, 10125 Turin, Italy

⁴ Laboratory of Chemistry and Materials Technology, General (Core) Department, National and Kapodistrian University of Athens, Psachna Campus, 34400 Evia, Greece; vasta@uoa.gr

* Correspondence: C.B.Anucha@ktu.edu.tr (C.B.A.); ilknuratlidil@ktu.edu.tr (I.A.)

Received: 5 November 2020; Accepted: 7 December 2020; Published: 10 December 2020



Abstract: This study investigated the synthesis of two different types of photocatalysts, namely, boron/sodium fluoride co-doped titanium dioxide (B/NaF-TiO₂), and its analogue, a dye-sensitized form of silicon-based axial methoxy substituted phthalocyanine (B/NaF-TiO₂SiPc). Structural and morphological characterizations were performed via X-ray diffraction (XRD); Fourier transform infra-red (FTIR); N₂ adsorption–desorption at 77 K by Brunauer–Emmett–Teller (BET) and Barrett, Joyner, and Halenda (BJH) methods; transmission electron microscopy (TEM); X-ray photoelectron spectroscopy (XPS); and UV–visible absorption spectroscopy. The estimated crystallite size of pure TiO₂ and pure B/NaF-TiO₂ was 24 nm, and that of B/NaF-TiO₂SiPc was 29 nm, whereas particle sizes determined by TEM were 25, 28, and 31 nm for pure TiO₂, B/NaF-TiO₂ and B/NaF-TiO₂SiPc respectively. No significant differences between B/NaF-TiO₂ and B/NaF-TiO₂SiPc were observed for surface area by (BET) analysis (13 m²/g) or total pore volume by the BJH application model (0.05 cm³/g). Energy band gap values obtained for B/NaF-TiO₂ and B/NaF-TiO₂SiPc were 3.10 and 2.90 eV respectively, lower than pure TiO₂ (3.17 eV). The photocatalytic activity of the synthesized materials was tested using carbamazepine (CBZ) as the model substrate. Carbamazepine removal after 4 h of irradiation was almost 100% for B/NaF-TiO₂ and 70% for B/NaF-TiO₂SiPc; however, the substrate mineralization proceeded slower, suggesting the presence of organic intermediates after the complete disappearance of the pollutant.

Keywords: photocatalysis; titania; phthalocyanine; boron/sodium fluoride; axial methoxy-substituted silicon phthalocyanine; carbamazepine; photocatalytic degradation; mineralization; contaminant of emerging concern

1. Introduction

Nowadays, environmental pollution remains one of the biggest and most challenging problems facing us with far reaching, devastating effects on the ecosystem, animals, and humans [1]. Among the synthetic molecules with potential impacts on the aquatic environment and the biosphere, pharmaceuticals and personal care products named contaminants of emerging concern (CECs), cause high concern due to their increasing use and refractoriness to conventional water treatments.

Recently, advanced oxidation processes (AOPs) have shown the ability to destroy organic pollutants in the water matrices, thereby transforming them into harmless compounds without the need for further post treatment processes [1,2].

Heterogeneous photocatalysis, in particular, by exploiting the use of titanium dioxide, allowed degrading completely different classes of pollutants, but TiO₂ activity could be further enhanced by adopting various strategies, such as metal and non-metal doping and anchorage with other narrower band gap semiconductors [3–6]. B-doped TiO₂ nano-powders obtained via sol–gel synthesis has been reported to be able to efficiently abate Methylene Blue (MB) thanks to an excellent combination of physico-chemical properties, including low band-gap energy, relatively high specific surface area, suitable surface morphology, and suitable surface charge [3]. The dye sensitization approach has been developed within the last decade to improve TiO₂ performance in photocatalysis. Compounds such as coumarin [7], porphyrin [8], and phthalocyanines (Pcs) [9] have been used as sensitizers to that end. Attention has been directed towards phthalocyanines and porphyrins because of their low cost and high efficiency [8]. Various metal/metalloid functionalized phthalocyanines, bearing more polar substituent groups on the benzene ring to modulate their water/organic solvent solubility, have been reported to enhance the TiO₂ efficiency towards the degradation of organic pollutants [10]. Erythromycin degradation has been achieved by the application of zinc phthalocyanine-modified titania nanoparticles prepared by a chemical impregnation method [11]. TiO₂ surface-modified with copper (II) phthalocyanine tetrasulphonic acid was successfully employed as a catalyst to obtain the photoinduced mineralization of organophosphate insecticide [12]. Copper (II) phthalocyanine/TiO₂ nanocomposites have been also applied for the photoreduction of Cr (VI) and microorganism disinfection under UV-A light (near UV–visible region of 365 nm wavelength) [13]. Boron doped TiO₂ nanotubes have been reported to be more active than the pristine TiO₂ [14]. Wu et al. reported enhanced photocatalytic efficiency of boron and carbon-modified TiO₂ prepared by sol–gel followed by a solvothermal process over the unmodified pure anatase TiO₂ for visible light degradation of AO7 organic dye [15]. Recently, we reported a study on the effect of manganese (III) phthalocyanine on the photocatalytic degradation of bisphenol A under 365 nm UV over ZnWO₄ [16].

Several studies have reported the synthesis and the photocatalytic applications of boron doped or sodium fluoride—or various other metal/non-metal/sensitizer modifiers in single or co-doped form—for enhanced photocatalytic activity of titania. To the best of our knowledge, boron and NaF co-doped titanium dioxide and its sensitized axial methoxy (–OCH₃)-functionalized silicon phthalocyanine form have not yet been reported. Here, we report for the first time promising results of TiO₂ co-doped with B and F (containing 3 wt.% each of boron and sodium fluoride dopants) with and without silicon phthalocyanine (1 wt.% of silicon phthalocyanine) synthesized via facile sol–gel method followed by wet deposition and their evaluation for the photocatalytic degradation of CBZ, a contaminant of emerging concern [15–20].

2. Materials and Methods

2.1. Reagents

All reagents used were of analytical grade and employed as purchased without further purification.

All reactions were carried out under dry and oxygen-free nitrogen atmosphere using Standard Schlenk techniques. 4-hydroxy-3-methoxybenzaldehyde (>99%), 5-aminopentanol, titanium isopropoxide (TiP), ethanol, boric acid, sodium fluoride, hydrochloric acid, 2-hydroxy tetrahydrofuran (THF), chloroform, acetone, potassium carbonate, toluene, dichloro silicon phthalocyanine (SiPcCl₂), dimethyl formamide (DMF), carbamazepine (>99%) were all purchased from Sigma Aldrich (Darmstadt, Hesse, Germany). Milli-Q water was used throughout the entire experiment for the photocatalytic studies.

2.2. Instrumentation and Methods

^1H -NMR and ^{13}C -NMR spectra were recorded on a Varian XL-200 NMR spectrophotometer (Bruker BioSpin MRI GmbH, Rheinstetten, Baden-Württemberg, Germany) in DMSO- d_6 , and chemical shifts reported (δ) relative to Me_4Si (TMS) as internal standard. FT-IR spectra were recorded on a Perkin-Elmer Spectrum one FT-IR spectrometer (Thermo Fisher Scientific, Leicestershire, UK). The mass spectra were measured with a Micromass Quattro LC/ULTIMA LC-MS/MS (Bruker Daltonik GmbH, Hamburg, Germany) for methoxy-substituted Schiff base compound 3, and MALDI-TOF MS spectrometers (Bruker Microflex LT, Bremen, Germany) for the Bis methoxy-substituted, Schiff base SiPc, compound 5. All experiments were performed in the positive ion mode. Melting points were measured on an electrothermal apparatus and uncorrected. Absorption spectra were recorded with a Shimadzu 2101 UV-Vis spectrophotometer.

XRD measurements were carried out using a Rigaku D/Max-IIIIC diffractometer (RIGAKU, Corp.; Tokyo, Japan) with Cu $K\alpha$ radiation ($\lambda = 0.1541$ nm) over the range $2\theta = 20$ – 60° at room temperature, operated at 35 kV and 25 mA at a $3^\circ/\text{min}$ scan speed.

N_2 adsorption–desorption isotherms were measured by BET on a Micromeritics ASAP 2010 system (Micromeritics, Norcross, GA, USA). The mesopore analysis was obtained with BJH method. TEM was carried out with FEITecnaïG2 Spirit (FEI, Hillsboro, OR, USA), and XPS data were obtained using a PHI 5000 VersaProbe Spectrometer (ULVAC-PHI, Inc.; Kanagawa, Japan) with an Al- $K\alpha$ radiation source.

2.3. Preparation and Characterization of Photocatalyst Materials

2.3.1. B/NaF-TiO₂

Facile modified sol–gel method was employed for the synthesis of the nanoparticles [21]. Briefly, 7.9 mL of titanium isopropoxide (TiP), used as a precursor of TiO₂, was introduced into 150 mL of ethanol in a glass flask. Keeping the mixture under stirring, 0.5 mL of deionized water, 0.064 g of both boric acid and sodium fluoride (corresponding to 3% of TiO₂ weight), and 220 μL of hydrochloric acid were added sequentially and the suspension was stirred for 8 h. The gel mixture was then dried at 80°C for 12 h and consequently calcined at 600°C for 2 h [22].

For pristine TiO₂, we followed the same procedure without the addition of the doping precursors.

2.3.2. B/NaF-TiO₂-SiPc Photocatalyst

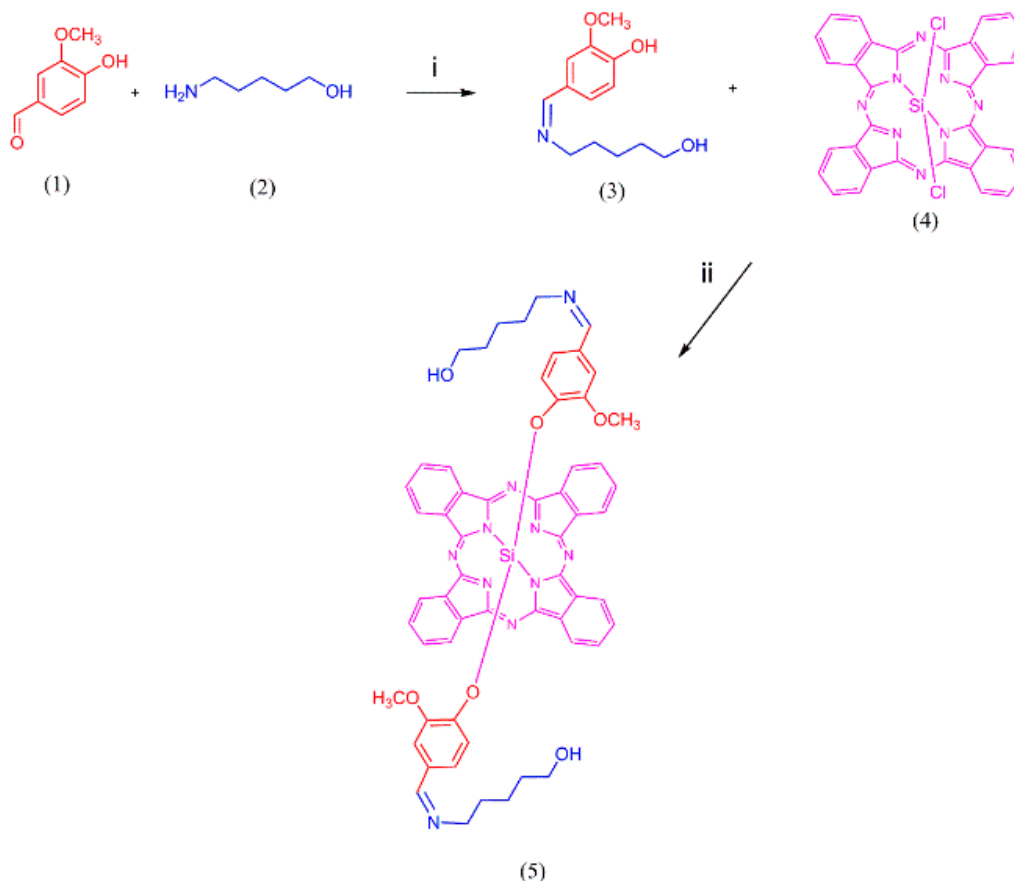
- Synthesis and characterization of axial substituted methoxy silicon phthalocyanines (SiPc)

As shown in Scheme 1, the synthesis of molecule (3) was the first step of the synthetic route of SiPc compound. Thus, firstly, (Z)-4-((5-hydroxypentylimino) methyl)-2-methoxyphenol (HPI-MP) (3) was obtained from the combination of substances (1) and (2). Subsequently, SiPc (5) was obtained from the addition of substances (3) and (4).

To obtain the axial methoxy substituted silicon phthalocyanine, 0.52 g of 4-hydroxy-3-methoxy benzaldehyde was dissolved in about 20 mL of dry tetrahydrofuran (THF). Subsequently, dry MgSO_4 (1.52 g; 10 mmol) was added. After stirring at room temperature under N_2 for 10 min, a solution of 5-amino pentanol (2) in 5 mL of dry THF (0.73 g; 4.81 mmol) was added dropwise. The reaction mixture was monitored by thin layer chromatography (TLC) and stirred at room temperature for 29 h. Excess undissolved MgSO_4 was filtered, washed twice with THF to recover any adsorbed useful product. Solvent was dried, and crude material purified by column over silica gel using chloroform: acetone (1mL: 0.1 mL v/v). Obtained yield was 28% [13,23–25].

Elemental Anal. Calc. for $\text{C}_{13}\text{H}_{19}\text{NO}_3$: C, 65.80; H, 8.07; N, 5.90. Found: C, 65.85; H, 8.01; N, 5.95. FT-IR (KBr, cm^{-1}): 3268 (Ar/aliphatic-OH), 3061 (=C-H), 2929 (CH_2), 1669 (C=N), 1598–1439 (C=C/C-C), 1331, 1165 (=C-O-C), 750, 710, 667 (1,2,4-tri substitution).

$^1\text{H-NMR}$ (DMSO- d_6), (δ :ppm): 11.41 (s, 1H/Ar-OH), 7.84 (bs, 1H/CH=N), 7.63–7.53 (m, 1H/Ar-H), 7.26–7.24 (m, 1H/Ar-H), 7.11 (s, 1H/Ar-H), 4.85 (s, 1H/Alip.-OH), 4.57–4.42 (m, 2H/CH₂), 3.58–3.49 (m, 2H/CH₂), 3.45–3.41 (m, 3H/OCH₃), 2.21 (s, 2H/CH₂), 1.45–1.42 (t, 2H/CH₂), 1.24 (s, 2H/CH₂).



i = dry MgSO_4 and dry THF

ii = dry K_2CO_3 and dry toluene

Scheme 1. The synthetic route of bis-methoxy-substituted Schiff base SiPc (5), and its building block components: (4-hydroxy-3-methoxy benzaldehyde (1), 5-amino pentanol (2), (Z)-4-((5-hydroxypentylimino) methyl)-2-methoxyphenol (HPI-MP) (3), and axial substituted dichloro silicon phthalocyanine (SiPcCl_2) (4).

$^{13}\text{C-NMR}$ (DMSO- d_6), (δ :ppm): 162.98 (CH=N), 135.41, 133.33, 130.91, 129.58, 128.32, 127.46, 72.99 (CH₃), 63.57 (CH₂), 62.03 (CH₂), 56.09 (CH₂), 54.68 (CH₂), 29.44 (CH₂). MS, (m/z): calculated; 237.31; found; 282.28 [$\text{M} + 2\text{Na}$]⁺.

- Bis methoxy-substituted Schiff based SiPc (5)

After 0.078 g of (3) was suspended in about 15 mL of dry toluene, 0.091 g of dry K_2CO_3 and 0.1 g of SiPcCl_2 (4) were added. Then, reaction mixture was heated at 70 °C, refluxed under N_2 atmosphere for about 24 h. Thereafter, solvent mixture was cooled to room temperature by complete evaporation. Obtained dark bluish-greenish residue was extracted several times with a chloroform-water mixture. With chloroform phase dried with MgSO_4 , obtained product (5) was purified by column over silica gel and in solid phase as a precipitate. Obtained yield was about 21% [13,23–25].

Elemental Anal. Calc. for $\text{C}_{58}\text{H}_{52}\text{N}_{10}\text{O}_6\text{Si}$: C, 68.76; H, 5.17; N, 13.82. Found: C, 68.92; H, 5.05; N, 13.65.

FT-IR (KBr, cm^{-1}): 3495 (aliphatic-OH), 3066 (=C-H), 2917–2850 (CH_2), 1641 (C=N), 1520–1463 (C=C/C-C), 1335, 1291 (=C-O-C), 759, 730, 702 (1,2,4-tri substitution).

$^1\text{H-NMR}$ (CDCl_3), (δ :ppm): 9.7–9.5 (m, 8H/Pc-H α), 8.4–8.3 (m, 8H/Pc-H β), 7.61 (bs, 2H/CH=N), 7.10–6.92 (m, 6H/Ar-H), 2.91–2.73 (m, 4H/ CH_2), 1.51–1.49 (m, 6H/ CH_3), 0.72 (bs, 4H/ CH_2), 0.32–0.25 (m, 8H/ CH_2), (−0.81) – (−1.04) (bs, 4H/ CH_2).

UV-vis (DMF) $\lambda_{\text{max/nm}}$ [$10^{-5} \epsilon$, $\text{dm}^3\text{mol}^{-1}\text{cm}^{-1}$]: 686 (4.89), 649 (3.95), 613 (4.05), 327 (4.63).

MS, (m/z): calculated; 1013.20 found; 1107.53 [$\text{M} + 2\text{K} + \text{H}_2\text{O}$] $^+$.

By wet deposition and employing DMF as solvent, about 1% of the weight of the synthesized methoxy substituted SiPc was anchored on the doped synthesized TiO_2 (synthesis described in Section 2.3.1) following heat treatment in an oven at 80 °C for 2 h. The synthesized materials were labelled B/NaF- TiO_2 and B/NaF- TiO_2 -SiPc and used in this study.

2.4. Photocatalytic Experiments

5 mL of aqueous dispersion containing 10 mgL^{-1} of carbamazepine and 1 gL^{-1} of catalyst was irradiated in stirred cylindrical closed cells (40 mm i.d. \times 25 mm high), made of Pyrex glass. A 1500 W Xenon lamp (Solarbox, CO. FO. MEGRA, Milan, Italy) equipped with a 340 nm cut-off filter was employed. The measured photonic flux of the simulated AM1 radiation (wavelength range: 340–400 nm) was ca. 1.4×10^{-5} Einsteins min^{-1} in the cell. Distance between lamp radiation source and sample was 20 cm with temperatures within the cells of ca. 50 °C [26–28].

Samples were drawn at the end of every pre-determined time of exposure, allowed to cool, filtered through a 0.45 μm hydrophobic PTFE membrane filter, and kept for analysis. The substrate degradation was monitored by HPLC using a Merck Hitachi instrument equipped with a L-6200 pump, AS-2000 Autosampler, and UV-Vis L-4200 detector. A column RP-C18 (Lichrosphere, 4 mm i.d. \times 125 mm long, from Merck) was used. The eluent used was acetonitrile/phosphate buffer (pH 2.9) 35/65% (*v/v*) and the flow rate 1.0 mL min^{-1} . The detector was set at 285 nm.

Dissolved organic carbon (DOC) evolution was followed using a Shimadzu 5000 TOC analyzer (catalytic oxidation on Pt at 680 °C). Calibration was achieved by injection of known amounts of potassium phthalate.

The separation and identification of intermediates were performed with a UFLC-SHIMADZU combined with QTRAP LC-MS/MS 3200 from SCIEX (Framingham, MA, USA). A Synergi 4 μm Fusion RP (Phenomenex, 50 \times 2 mm) was employed using a mobile phase of 0.01% formic acid (eluent A) and acetonitrile (eluent B) with a flow rate of 0.4 mL min^{-1} . The column oven was set at 40 °C. The following gradient mobile phase composition was adopted: from 95/5 (*v/v* A/B) to 0/100 in 15 min, which was held for 3 min and followed by a re-equilibration of the column to the starting conditions. An injection volume of 10 μL was used for all samples. Electrospray ionization (ESI) was applied in positive ion mode (enhanced mass resolution, 50–600 *m/z* range) and the source parameters were as follows: ionization voltage was set at 2000 eV, ion source temperature was fixed to 550 °C, curtain gas was 20 psi, and collision gas was set to a high temperature—ion spray gases 1 and 2 were set at 60 and 70 psi respectively.

3. Results and Discussion

3.1. Synthesis and Characterization of the Methoxy-Substituted Silicon Phthalocyanine (SiPc)

3.1.1. Synthesis of the Methoxy-Substituted Silicon Phthalocyanine (SiPc)

The synthetic route followed for the preparation of the methoxy-substituted Schiff base (3) and its corresponding silicon phthalocyanine (5) is shown in Scheme 1. The substituted Schiff base (3) was obtained from the condensation of the starting compounds (1 and 2) [23]. The resulting compound (5), the methoxy-substituted SiPc, was synthesized by the reaction between compound (3) and (4) in dry toluene in the presence of K_2CO_3 [24].

3.1.2. Characterization of SiPc

The characterization of the structures of new compounds has been achieved by a combination of ^1H and ^{13}C -NMR, FT-IR, UV-Vis spectroscopy, and mass spectral data.

The expected structure of compound (3) was confirmed by the following signals:

(i) FT-IR spectrum of compound (3) (Figure S1): the absence of the $-\text{NH}_2$ stretching vibration of the compound (2), and $-\text{CH}=\text{O}$ stretching vibration of the compound (1) with the appearance of the vibration peak of the imine compound (3); (ii) ^1H -NMR spectrum (Figure S2): the formation of the imine structure at 7.84 ppm by combining the carbonyl and amine groups; (iii) ^{13}C -NMR spectrum (Figure S3): the signals observed at 162.98 ppm of azomethine carbon on imine fragment and the signals at 63.57, 62.03, 56.09, 54.68, and 29.44 ppm related to the presence of aliphatic carbons in the structure; (iv) ^1H -NMR spectrum of compound (3) in D_2O (Figure S4): the disappearance of aromatic OH at 11.41 ppm and aliphatic OH at 4.85 ppm [13,29,30]; and (v) mass spectral analysis (Figure S5): the presence of the signal at m/z 282.28 related to $[\text{M} + 2\text{Na}]^+$ ion peak.

The IR absorption spectrum of methoxy-substituted Schiff based SiPc (5) was similar to the precursor (3). Modification of the structure (3) into silicon phthalocyanine (5) led to the disappearance of the stretching vibration 3225 cm^{-1} —aromatic $-\text{OH}$ group (Figure S6).

In the ^1H -NMR spectrum (Figure S7), the phthalocyanine ring proton resonances appeared as multiplets integrating each as 8H at (9.70–9.50)/(8.40–8.30) ppm for SiPc (5) α and β protons. Due to magnetic anisotropy of phthalocyanine ring [25,31], the resonance between -0.81 and -1.04 ppm for (5) was assigned to submethyl protons of $\text{CH}=\text{N}-\text{CH}_2$, which were the most shielded protons. In the MALDI-TOF MS spectrum of (5), the molecular ion peak was observed at 1107.53 $[\text{M} + 2\text{K} + \text{H}_2\text{O}]^+$ (Figure S8).

3.1.3. UV-Vis Absorption of the Methoxy-Substituted Silicon Phthalocyanine

The major problem encountered in phthalocyanine applications is their extremely poor solubility in commonly used solvents, especially water. To overcome this problem, some methods, such as the preparation of their cationic or anionic derivatives, and the axial or peripheral substitution to phthalocyanine ring, can be used [32]. In our study, an axially substituted silicon phthalocyanine (5, Scheme 1) was synthesized for increasing its solubility in polar organic solvents. This compound has proven to be soluble in common organic solvents such as THF, dichloromethane, chloroform, DMF, and DMSO [13,24]. Generally, phthalocyanine derivatives give two main absorption bands named B and Q at around 350 and 670 nm, respectively. While the Q band represents the $\pi \rightarrow \pi^*$ transition between HOMO and LUMO, the B band is responsible for the transition from deeper level π orbitals to LUMO [33]. In this study, the UV-Vis spectrum of the synthesized silicon phthalocyanine (Figure 1) was recorded in DMF 1×10^{-5} M. The Q bands of the SiPc were observed at 686, 649 and 613 nm, whereas the B band was observed at 327 nm. The investigated silicon phthalocyanine (5) showed a single narrow and intense Q band absorption due to its D_{4h} symmetry [13,24]. Generally, the absence of either a red-shift or a blue-shift of the Q band excludes the formation of aggregated species in solution.

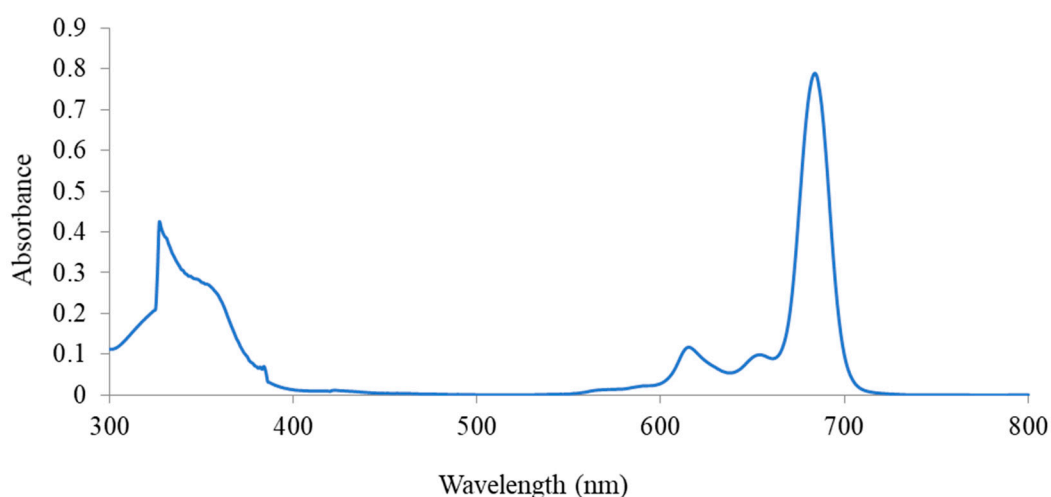


Figure 1. UV–Vis spectrum of silicon phthalocyanine (5) in DMF at 1×10^{-5} M.

3.2. Photocatalyst Characterization

3.2.1. X-Ray Diffraction (XRD) Analysis

The Figure 2 shows the XRD patterns of all synthesized catalysts. Diffraction angles 2θ of 25.2° , 36.88° , 37.67° , 38.5° , 48.0° , 53.78° , and 54.90° were attributed to the (101), (103), (004), (112), (200), (105), and (211) planes of TiO_2 anatase phase, respectively, according to JCPDS cart# 01-071-1168. This confirms that neither the doping with boron or sodium fluoride, nor the anchorage of silicon phthalocyanine on the TiO_2 catalyst affects in a significant way the crystalline structures of the synthesized materials. However, pure TiO_2 shows the presence of a large halo centered at 25° , indicating the presence of short-range order domains, i.e., the presence of some amorphous-like TiO_2 phase. In addition, some small differences between modified and non-modified samples are well represented in the inset of Figure 2. The doping and the surface modification cause the shift of the main signal at $2\theta = 25^\circ$ to higher angles as the result of the insertion of boron (characterized by a small ionic radius) in the TiO_2 crystalline cell. The band width decrease indicates a slight increase of the size of the crystalline domains.

Crystalline domain sizes (D) of undoped and co-doped catalyst powders were determined through Debye–Scherrer expression:

$$D_{hkl} = 0.9\lambda/\beta_{hkl}\cos\theta \quad (1)$$

where $\lambda = 1.54059\text{\AA}$ is the wavelength of the Cu/K- α source, β is the integral breadth of the XRD peaks depending on the width of the particular hkl plane and taken at full width at half height maximum (FWHM) in degrees, θ is the diffraction angle obtained from the XRD data of the strongest reflection, and K is the shape factor kept at constant value of 0.9. Calculated crystallite size values have been obtained using Equation (1) and in reference to the JCPDS# 01-071-1168 TiO_2 anatase [3,34].

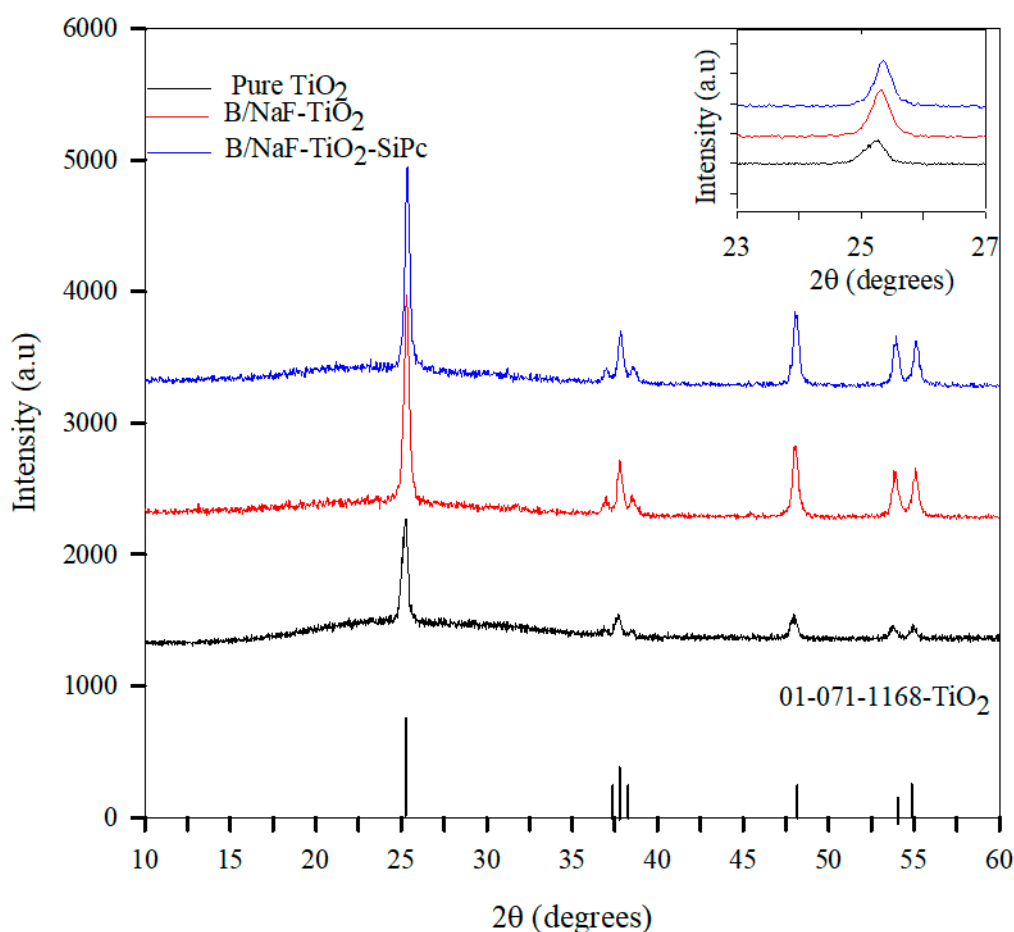


Figure 2. XRD patterns of TiO₂; B/NaF-TiO₂ and B/NaF-TiO₂-SiPc. In the inset, magnification of the main TiO₂ signal at 2θ = 25°.

Obtained data are listed in Table 1: as expected, the crystal size increases in the order pure TiO₂ ≈ B/NaF-TiO₂ < B/NaF-TiO₂SiPc.

Table 1. Morphologic and structural characterizations of the synthesized materials.

Catalyst	S _{BET} (m ² /g)	^a V _{pore} (cm ³ /g)	^b CS, Crystallite Size (nm)	^c d _{TEM} , Particle Size (nm)
Pure TiO ₂	~ 1	<0.01	24	25
B/NaF-TiO ₂	13	0.05	24	28
B/NaFTiO ₂ SiPc	13	0.05	29	31

^a BJH adsorption pore volume, ^b Debye–Scherrer equation, ^c particle size estimated by TEM.

3.2.2. N₂ Adsorption–Desorption at 77K (BET and BJH Model Application)

The adsorption isotherms reported in Figure 3 can be classified as type IV [35,36], with the H3 hysteresis loop indicating the existence of mesopores [36], as supported by Figure S9 for both B/NaF-TiO₂ and B/NaF-TiO₂-SiPc catalysts. The isotherm of pure TiO₂ showed a limited adsorption with respect to the others, indicating a smaller surface area and negligible porosity. The BET (Brunauer, Emmet, and Teller) specific surface area and total pore volume are reported in Table 1. In all cases, the specific surface area (S_{BET}) of the modified material in question showed a significant increase with respect to pristine TiO₂. The pore structure changes in both B/NaF-TiO₂ and B/NaF-TiO₂SiPc are attributed to the addition of B/NaF [6]. Additional effects of both B/NaF and SiPc also reflected

the slight increase in particle size for B/NaF-TiO₂ and B/NaF-TiO₂SiPc over pure TiO₂ (Table 1). Further discussion on the effect of F and B is provided in Section 3.2.5.

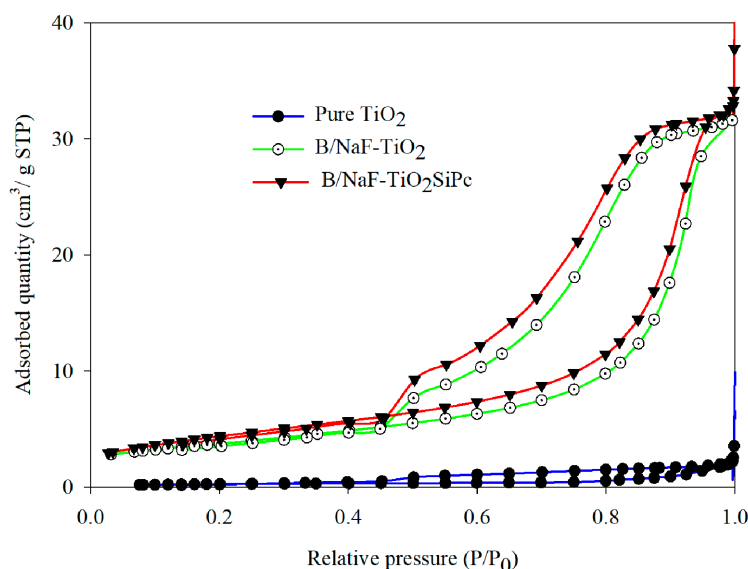


Figure 3. N₂ adsorption–desorption isotherms of synthesized materials.

3.2.3. Fourier Transform Infrared (FTIR) Spectroscopy Analysis

The spectra of the three materials presented in Figure 4 are remarkably similar to each other. They show the typical trend expected of TiO₂ anatase. The introduction of the dopant does not affect the shape of the pristine TiO₂, whereas the surface functionalization with the SiPc allows for an increase in the hydrophilicity of the sample, as evidenced by the presence of δ_{HOH} signal of water molecules at 1630 cm⁻¹ and the δ_{OH} signal of hydroxyl groups at 3700 cm⁻¹, and by the increase of the $\delta_{\text{Ti-OH}}$ band at 1068 cm⁻¹. In addition, the signals that appeared at around 3000 cm⁻¹ in all the samples have been attributed to –CH vibrational bonds and become more intense when SiPc is present [37].

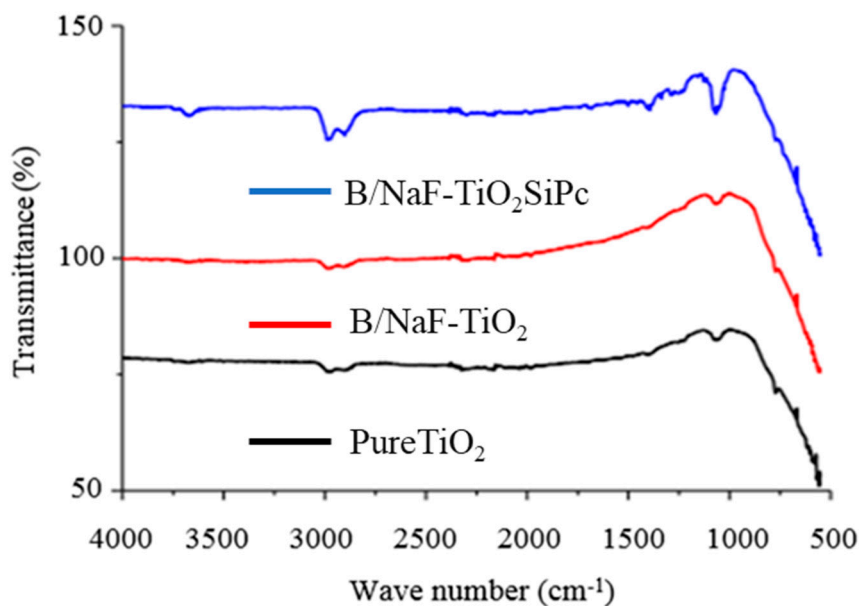


Figure 4. FTIR spectra of pure TiO₂; B/NaF-TiO₂ and B/NaF-TiO₂-SiPc.

3.2.4. Transmission Electron Microscopy (TEM)

From the TEM images of synthesized catalysts reported in the Figure 5, all samples show similar morphologies: the sizes of primary particles are in the range 20–50 nm (Table 1), though B/NaF-TiO₂ reveals in some cases large spherical nanoparticles of sometimes more than 200 nm in diameter as well. The nanoparticles appear randomly more spherical in the case of B/NaF-TiO₂, whereas B/NaF-TiO₂SiPc shows nanopolyhedral shape [35,36]. However, pure TiO₂ is clearly of a bulkier nature consisting of much larger and more agglomerated particles.

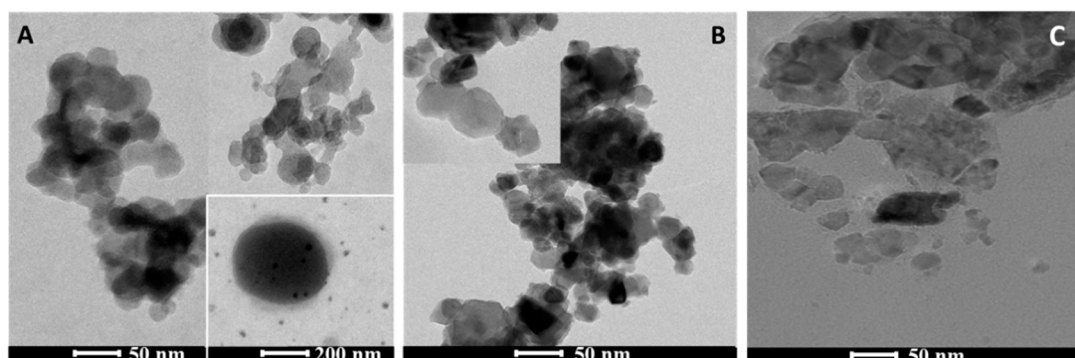


Figure 5. TEM image: (A) B/NaF-TiO₂; (B) B/NaF-TiO₂SiPc; and (C) pure TiO₂.

3.2.5. X-Ray Photoelectron Spectroscopy (XPS) Analysis

To elucidate the chemical surface compositions of samples, XPS analysis was performed. The survey spectra of B/NaF-TiO₂ and B/NaF-TiO₂SiPc revealed, as expected elemental, chemical components of the samples (Figures 6I and 7II). Both spectral image signals showed the same elemental composition, except for the N and Si obtained by the B/NaF-TiO₂SiPc sample after Pc sensitization. As expected, binding energy signals related to Ti 2p with its associated Ti 2p_{3/2} and Ti 2p_{1/2} were registered at 458.1 and 463.7 eV respectively; and O 1s, B 1s, C 1s, Na 1s, and F 1s, comprising the main and deconvoluted spectra, were recorded at (529.3, 531.34 eV), (191.5, 193.2 eV), (284.4, 286.9 eV), (1071.5 eV), and (683.2, 685.5 eV), respectively, for the B/NaF-TiO₂ (Figure 6I,a–f).

In the same vein, for the B/NaF-TiO₂SiPc, Ti 2p with its associated Ti 2p_{3/2} and Ti 2p_{1/2} were recorded at binding energies, 458.5 and 464.0 eV respectively. O 1s, B 1s, C 1s, Na 1s, F 1s, the other elements of N 1s, and (Si 2p_{1/2}, Si-O_x, or Si-N) following Pc sensitization in the obtained samples were recorded at binding energies of (529.7, 531.6 eV), (192.3, 193.8 eV), (284.1, 286.90 eV), (1071.3, 1069.8 eV), (683.6, 684.5 eV), (398.6 eV), and (100.0, 102.5 eV) comprising the main and deconvoluted spectra respectively (Figure 7II,a–h). Reported O 1s and B 1s structures for each of the photocatalysts samples at their registered binding energies, respectively, indicated the presence of C=O (531.3 eV), C_{aliphatic}-O (532.6 eV) and C_{aromatic}-O (531.1 eV), and B-Ti-O and B₂O₃ components, in agreement with the literature [6,38–41]. Other expected signals: C 1s (284.3 eV), Na 1s (1071.5 eV), F 1s (683.2 eV), N 1s (398.6 eV), and Si 2p of either Si 2p_{1/2} or Si-O_x/Si-N at (100.0 eV, 102.5 eV) were recognized in the spectra (Figure 6I,a–f and Figure 7II,a–h); C 1s peaks of the samples at 286.9 and 286.0 eV are characteristic of the oxygen bond specie of C–O, previously reported with C incorporation into the TiO₂ lattice in the form of CO [6,41–43]. Contributions of the F 1s region due to physically adsorbed F[−] ions on the surface of TiO₂ and the ones in solid solution from TiO_{2-x}F_x formed by the substitution of oxygen into the TiO₂ lattice, and possibly in situ HF formation, may have affected the development of porosity, contrary to the pure TiO₂ [6] (Figure 6I,a–f and Figure 7II,a–h). The substitution of the O^{2−} sites by F[−] ions creates a charge imbalance and respective defects. Such additional defects may be responsible for the existence of new weakly bound surface oxygen species not available in pure TiO₂. TiO₂, as studied thoroughly in the literature, revealed O1s signals at 529 and 531 eV attributed to Ti-O and -OH groups respectively [6,30,36].

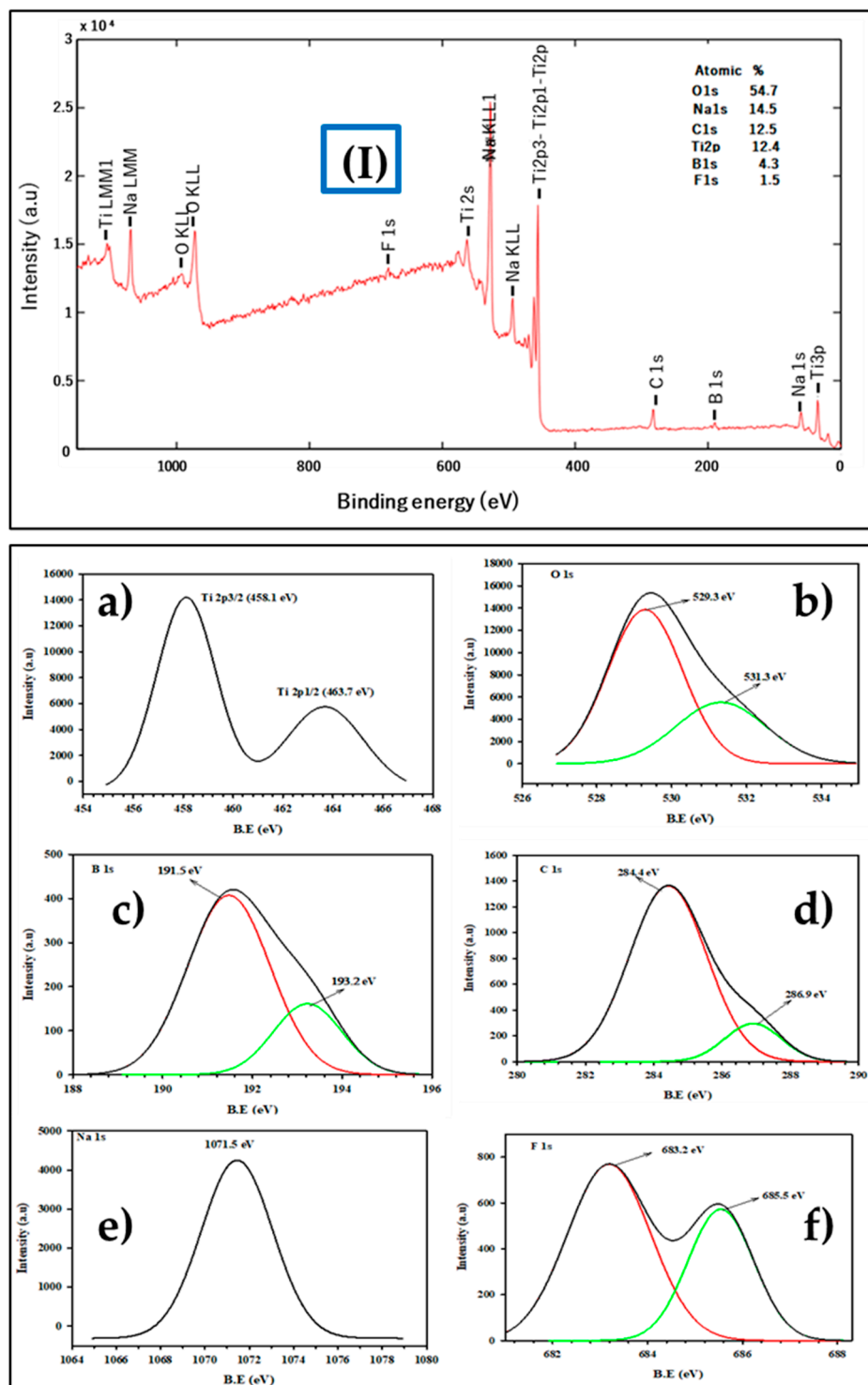


Figure 6. (I). XPS spectrum and corresponding deconvoluted elemental spectra of (a) Ti 2p; (b) O 1s; (c) B 1s; (d) C 1s; (e) Na 1s; and (f) F 1s for B/NaF-TiO₂ photocatalyst.

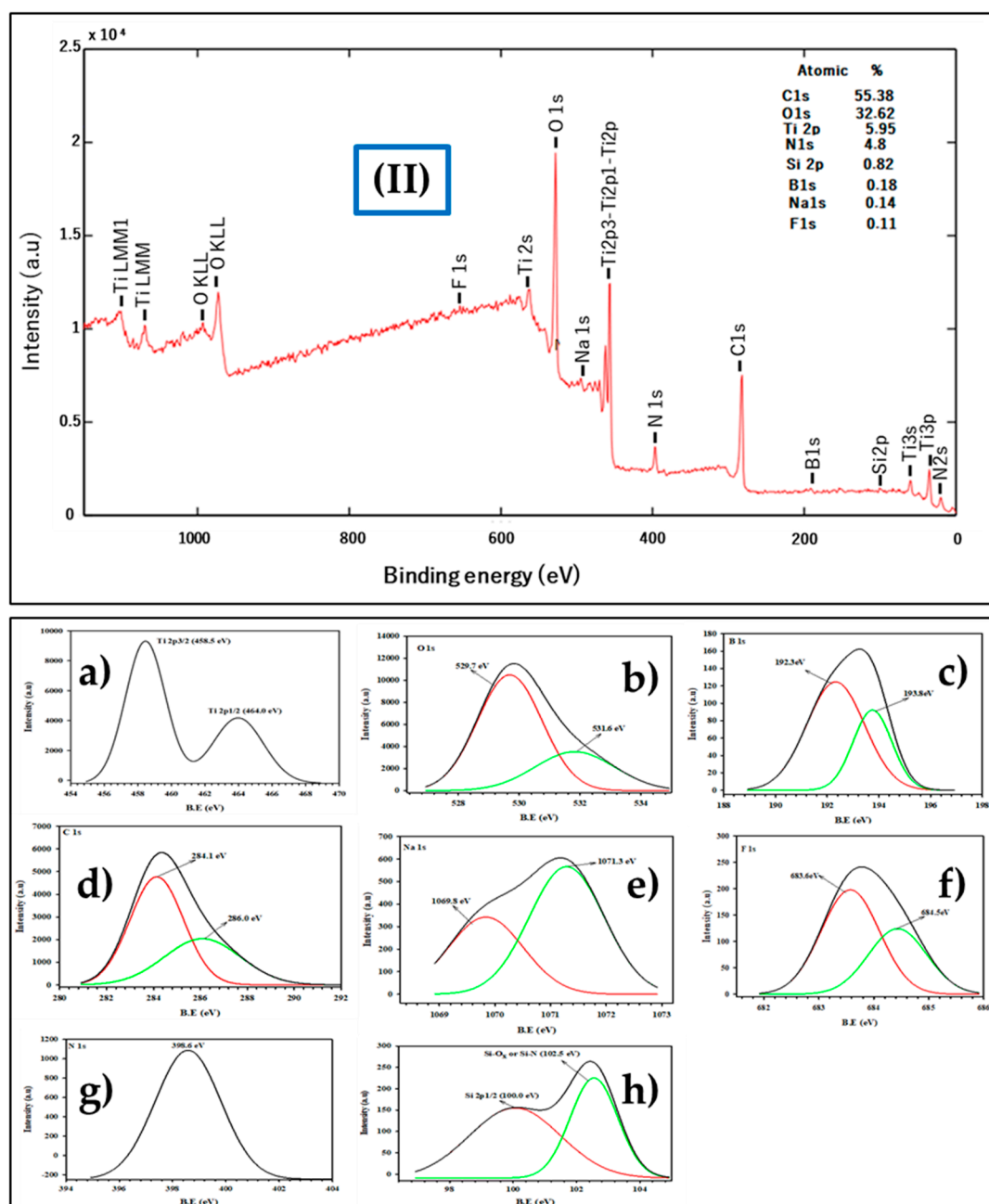


Figure 7. (II). XPS spectrum and corresponding deconvoluted elemental spectra of (a) Ti 2p; (b) O 1s; (c) B 1s; (d) C 1s; (e) Na 1s; (f) F 1s; (g) N 1s; and (h) Si 2p for B/NaF-TiO₂-SiPc photocatalyst.

On a general note, worth mentioning is the shift in binding energies in the range of 0.2–1 eV amongst the recorded elemental spectral signals of B/NaF-TiO₂ and B/NaF-TiO₂SiPc samples following B/NaF and SiPc modification of TiO₂ to obtain them. These shifts might be ascribed to changes in the physical and or chemical environments of the analyzed species, as they no longer maintained the same local bonding environment in terms of their formal oxidation states, nearest neighbor atomic element identity, and inter atomic bonding hybridizations [40]. Such variations can be responsible for significantly modified catalytic activity seen with these samples over pure TiO₂.

3.2.6. Light Absorption and Energy Band Gap Structural Analysis

UV–Vis absorption spectroscopic values of the catalysts with respect to the pure TiO₂ were registered and the corresponding wavelength harmonized using the Tauc’s plot to calculate the indirect

energy band gap. The Tauc’s indirect energy band gap expression in Equation (2) has been employed to obtain the energy band gap values.

$$(\alpha h\nu) = C(h\nu - E_g)^n \tag{2}$$

where α represents semiconductor optical absorption coefficient close to the band gap energy, $h\nu$ the energy of incident photons, C light speed, E_g the band gap energy, and n the number of transitions, which is $\frac{1}{2}$ in our case.

From the data reported in the Figure 8A,B, the values of the energy band gap (eV) were determined for the synthesized catalysts. It is evident that the B/NaF co-doping and the SiPc sensitizer reduce the energy band gap compared to that obtained for the pure TiO₂. Energy band gap data values of 3.17, 3.10, and 2.90 eV [41] were obtained for pure TiO₂, B/NaF-TiO₂, and B/NaF-TiO₂SiPc samples.

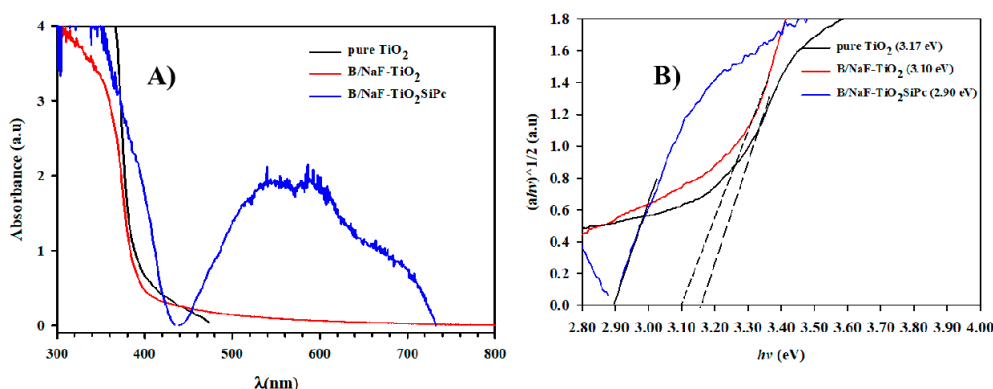


Figure 8. (A) UV-Vis spectra and (B) energy band of pure TiO₂; B/NaF-TiO₂ and B/NaF-TiO₂SiPc.

3.3. Photocatalytic Activity

The photocatalytic efficiency of the synthesized semiconductors was tested toward the abatement of CBZ—chosen as the target pollutant—while employing pure TiO₂ as the reference catalyst. Preliminary tests performed in the dark showed negligible degradation and absorption of the CBZ on the catalysts in the considered time window; under the chosen experimental conditions, direct photolysis induced almost 20% CBZ disappearance after the 4 h irradiation (Figure 9). The catalysts B/NaF-TiO₂ and B/NaF-TiO₂SiPc showed higher degradation efficiency under UV light illumination than pure TiO₂, and the best performance was obtained with B/NaF-TiO₂—able to achieve the complete disappearance of CBZ after 4 h (Figure 9). At the same time of irradiation, almost 20% of CBZ still remained in the presence of B/NaF-TiO₂SiPc.

The Figure 9 reports linear plots obtained by fitting the degradation data with the following equation:

$$-\ln(C/C_0) = k_{app}t \tag{3}$$

where C_0 is initial concentration and C is concentration at the irradiation time t ; in all cases, good linearity is observed. The constant rate values (k_{app}) obtained through Equation (1) were 1.1 h⁻¹ for B/NaF-TiO₂, 0.4 h⁻¹ for B/NaF-TiO₂SiPc, and 0.1 h⁻¹ for pure TiO₂.

The synergistic effect of TiO₂ doping with boron and sodium fluoride [44,45] and SiPc sensitization improved the photocatalytic activity of the synthesized catalysts.

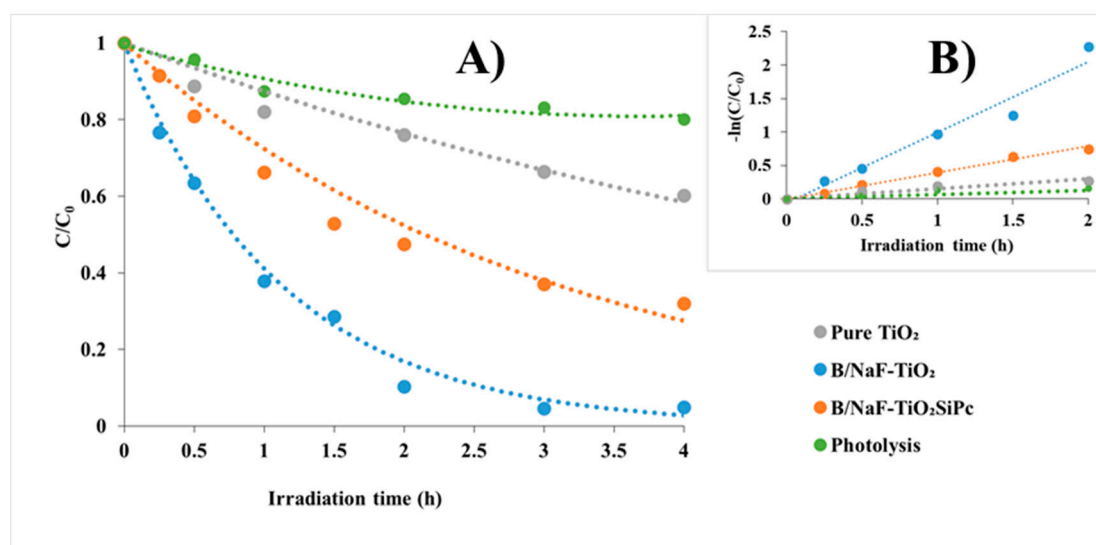


Figure 9. Degradation of CBZ: (A) under UV light irradiation and photolysis; and (B) apparent first order rate constant (k_{app}) [$C_0 = 10 \text{ mgL}^{-1}$; catalyst amount = 1 gL^{-1} ; pH = 6.5–6.9].

Concerning the co-doping effects, the use of boron does not affect the photocatalytic activity of pristine TiO_2 , thereby reducing the band gap, as it does not overlap the conduction band of TiO_2 [6,41], but it may instead affect the TiO_2 structure, leading to an increase in specific surface area. Such B-induced structural local disordering may increase also the defect population with a consequent positive effect on photocatalytic properties [36,41]. On the other hand, a fluorine atom can replace the oxygen atom of titanium dioxide, creating surface oxygen defects and vacancies that possibly trigger electron/hole recombination [3,6]. This phenomenon was not evident with B/NaF- TiO_2 SiPc compared with B/NaF- TiO_2 due to the presence of the electron withdrawing group (EWG) of the silicon phthalocyanine compound (5) [46,47].

The dissolved organic carbon (DOC) measurements were carried out as well, in order to assess the mineralization of CBZ and its transformation products during the irradiation in the presence of investigated catalysts. Figure 10 reports the trend of total organic carbon during the photocatalytic treatment in the presence of the synthesized catalysts. For B/NaF- TiO_2 , the complete mineralization of the molecule was not achieved, and the residual DOC (ca. 70% of the initial content) detected even after 4 h irradiation suggests the presence of organic intermediates after the complete disappearance of the pollutant. For B/NaF- TiO_2 SiPc at the end of irradiation process, a decrease of about 20% of initial DOC can be noticed, in agreement with a lesser photocatalytic efficiency.

The release of nitrogen with the formation of nitrate, nitrite, and ammonium occurred throughout the process. The initial delay time observed for both catalysts could be justified by the formation in the first steps of CBZ degradation of transformation products still containing nitrogen. Nitrite and nitrate concentrations were detected at negligible concentrations, confirming that the nitrogen mineralization leads to the formation of ammonium ions, as already reported in the literature for the CBZ photocatalytic degradation [48,49]. In both cases, the nitrogen mass balance did not reach the stoichiometric concentration after 4 h of irradiation; the percentage of total nitrogen transformed into inorganic products was about 25–30%. The DOC and end-inorganic products' evolutions in the presence of TiO_2 were not reported, as the issue has already been discussed in previous literature [48].

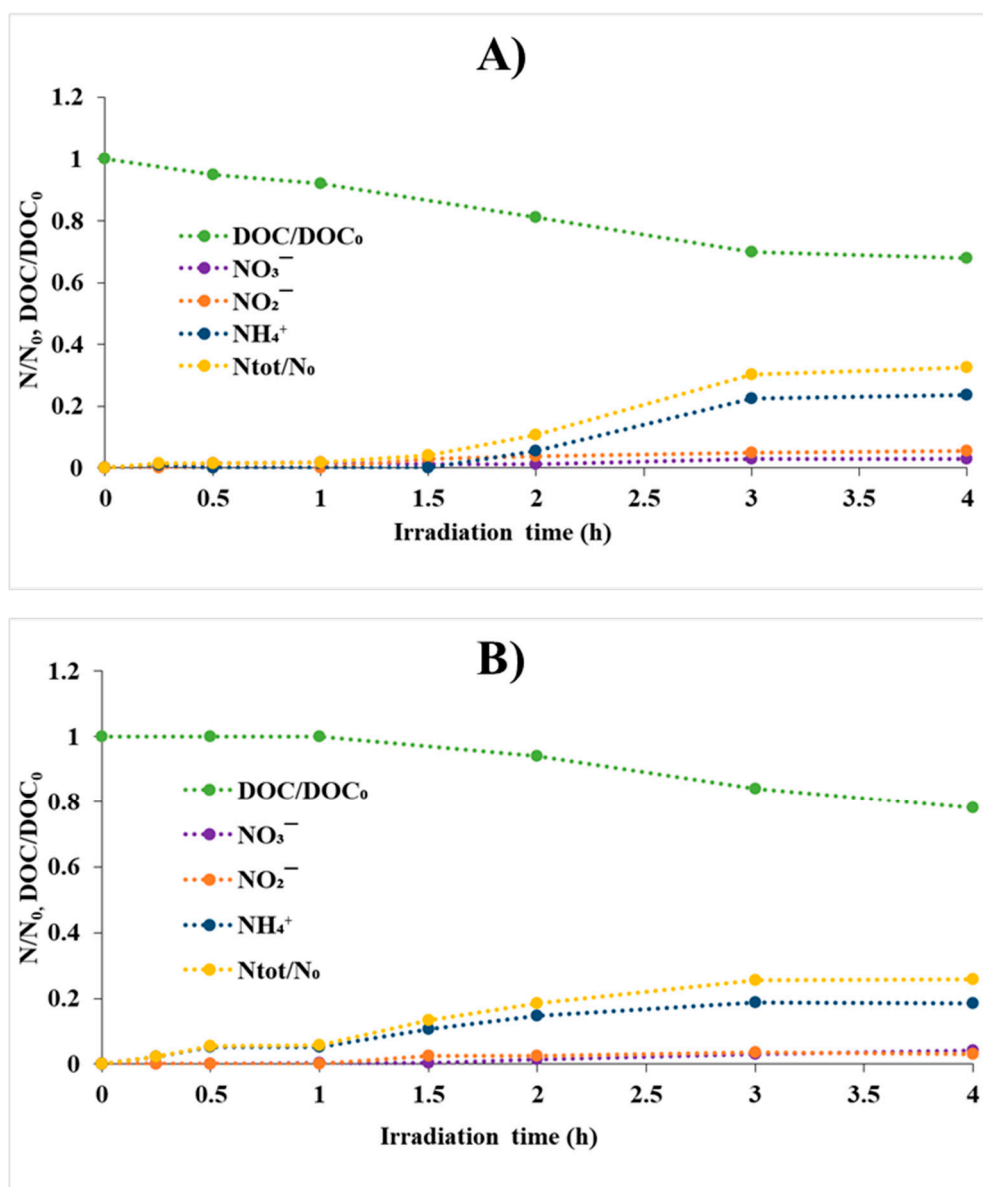


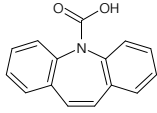
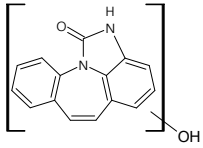
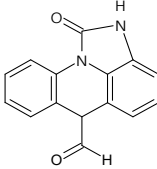
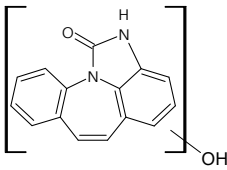
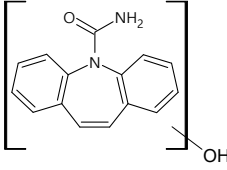
Figure 10. DOC, nitrate, nitrite, and ammonium evolution as functions of degradation time of CBZ (10 mgL⁻¹) in the presence of (A) B/NaF-TiO₂ (1 gL⁻¹) and (B) B/NaF-TiO₂SiPc (1 gL⁻¹).

3.4. Transformation Products

The identification of the intermediates produced during the CBZ degradation was performed by LC/MS analysis, and the obtained results are collected in Table 2, while Figures S10 and S11 of SI show the evolution profiles over time for the transformation products observed in the presence of the two catalysts (B/NaF-TiO₂ and B/NaF-TiO₂-SiPc). Seven main signals were detected in the sample prepared in the presence of B/NaF-TiO₂ (see Table 2).

Four species at 253 *m/z* (253_A, B, C, and D) were detected and can be postulated to be formed via CBZ monohydroxylation, in agreement with literature data [48]. No information useful for distinguishing the different isomers was obtained. The transformation products 251_A and 251_C can be justified by assuming a hydroxylation and an intramolecular cyclization. Conversely, for the intermediate 251_B, the presence in MS² spectrum of the product ion at 180 *m/z* (acridine) as a base peak suggests a monohydroxylation and an oxidation with ring contraction, as also concluded in the literature [48].

Table 2. List of $[M-H]^+$ and proposed structures for CBZ transformation products formed in the presence of B/NaF-TiO₂.

$[M-H]^+$	Label	Retention Time (min)	Chemical Structure
237	237	5.96	
251	251_A	3.72	
	251_B	4.43	
	251_C	4.69	
253	253_A	4.29	
	253_B	4.90	
	253_C	5.20	
	253_D	5.35	

The evolution time for each intermediate follows a bell-shaped profile reaching a maximum after 30 min, and their disappearance was observed within 2 h of irradiation. Considering the residual DOC content and the partial release of nitrogen as inorganic ions, we can hypothesize the formation of other transformation products of lower molecular weight still containing the nitrogen, not detected under our experimental conditions.

When the B/NaF-TiO₂SiPc was employed, we observed the formation of the same intermediates, with 251_A and 253_A as the only exceptions.

In this case, the products reached the maximum yield after 60 min of irradiation. A different behavior was observed for the 251_B, whose presence was noticed only after 240 min of treatment. The complete abatement of these intermediates was not achieved with B/NaF-TiO₂SiPc in the investigated time window, in agreement with the slight DOC removal previously discussed.

4. Conclusions

Two photocatalysts, namely, B/NaF-TiO₂ and B/NaF-TiO₂SiPc, obtained via sol-gel method and Schiff base process for the SiPc component, were successfully synthesized. To enhance photocatalytic activity, boron and sodium fluoride were introduced onto pure TiO₂ for the first time as co-dopants. Silicon-based phthalocyanine with a re-engineered bis axial methoxy (-OCH₃) functionalized group was designed, synthesized, and anchored successfully onto the co-doped-TiO₂ by a wet deposition method as the dye sensitizer. The new compounds/photocatalyst materials were characterized by combining several spectroscopic and structural/morphological techniques, including ¹H/¹³C-NMR,

MALDI-TOF, XRD, FT-IR, N₂ adsorption–desorption isotherm by BET and BJH application model, TEM, XPS, and UV–Vis spectroscopy. The two modified materials exhibited increases in crystal and particle size and specific surface area, and reductions in energy band gap compared to pristine TiO₂. It was inferred that B and F dopants were able to interstitially weave into the TiO₂ lattice, forming Ti–O–B and Ti–O–F bonds respectively, creating oxygen vacancy with such defects, leading to availability of more surface oxygen species responsible for the enhanced photocatalytic activity of the two materials. Both B/NaF-TiO₂ and B/NaF-TiO₂SiPc showed better performances with respect to pure TiO₂ under UV light irradiation, with B/NaF-TiO₂ achieving the complete removal of the pollutant in 4 h. Furthermore, the successful dye sensitization strategy of B/NaF-TiO₂ with a SiPc tailored with a hydrophilic functional group in the axial position of the macrocyclic compound also showed increased photocatalytic activity over CBZ compared to unmodified TiO₂. Such a double modification strategy of doping and sensitizing of TiO₂ resulted in photocatalytic efficiency improvement via low cost and straight forward methods such as sol–gel and wet deposition. The photocatalysts B/NaF-TiO₂ and B/NaF-TiO₂SiPc are promising, and therefore will be further tested in our future studies for the abatement of other CECs. In particular, in the near future, B/NaF-TiO₂SiPc material will be further investigated by exploiting the electrochemical advantages of the coupled, enhanced, hydrophilic axial-bis-methoxy-SiPc for visible and/or near infrared (NIR) photocatalytic activity. Additionally, we wish to improve understanding of the influences of substituent functional group positioning—axial or peripheral—on the macrocyclic compound, thereby getting insights on the resulting effects on the photocatalytic activities of the modified materials; and assessing their charge transfer mechanisms will be interesting.

Supplementary Materials: Supplementary materials can be found at <http://www.mdpi.com/2297-8739/7/4/71/s1>. Figure S1. FT-IR spectrum of compound (3). Figure S2. ¹H-NMR spectrum of compound (3) in DMSO-d₆. Figure S3. ¹³C-NMR spectrum of compound (3) in DMSO-d₆. Figure S4. ¹H-NMR spectrum of compound (3) in DMSO-d₆ / D₂O. Figure S5. ESI-MS spectrum of compound (3). Figure S6. FT-IR spectrum of compound (5). Figure S7. ¹H-NMR spectrum of compound (5) in CDCl₃. Figure S8. MALDI-TOF MS spectrum of compound (5). Figure S9. BJH pore size distribution for synthesized photocatalyst materials. Figure S10. Evolution of photodegraded products detected in the presence of B/NaF-TiO₂. Figure S11. Evolution of photodegraded products detected in the presence of B/NaF-TiO₂SiPc.

Author Contributions: C.B.A. assisted with material synthesis, performed the experiments, and prepared the original draft of the manuscript. I.A. supervised the worked, assisted with the work plan, and performed the in-house manuscript review. D.F. supervised part of the work and reviewed the manuscript. I.D. synthesized and characterized the phthalocyanine materials used in this work and reviewed the manuscript. P.C. was involved in planning the work and reviewed the manuscript. V.N.S. supervised part of the work and reviewed the manuscript. E.B. synthesized the photocatalytic materials, characterized them, supervised, and was involved in manuscript review. G.M. assisted with the N₂ adsorption–desorption isotherm measurements and reviewed the manuscript. All authors have read and agreed to the published version of the manuscript.

Funding: This work has received funding from the European Union’s Horizon 2020 research and innovation programme under the Marie Skłodowska–Curie grant number: 765860 (AQUALity).

Acknowledgments: The authors wish to acknowledge the contribution of Compagnia di San Paolo supplied under the pluriannual Convention between the University of Torino and Compagnia di San Paolo (ex-post projects).

Conflicts of Interest: The authors declare no conflict of interest.

References

1. Saracino, M.; (Institute for Organic Synthesis and Photoreactivity (ISOF), Italian National Research Council (CNR), Bologna, Emilia Romagna, Italy); Salvatore, S.E.; (Institute for Organic Synthesis and Photoreactivity (ISOF), Italian National Research Council (CNR), Bologna, Emilia Romagna, Italy); Zaneli, A.; (Institute for Organic Synthesis and Photoreactivity (ISOF), Italian National Research Council (CNR), Bologna, E. Romagna, Italy). *Chemistry and Industry. Scientific Communication*, 1997.
2. Jimenez-Hogaldo, C.; Chrimatopoulos, C.; Stathopoulos, V.; Sakkas, V. Extraction and HPLC-UV-Vis/DAD to Determine Antidepressant Drugs in Environmental Aqueous Samples. *Separations* **2020**, *7*, 39. [[CrossRef](#)]

3. Ganesh, I. Surface Structural Energy Band Gap and Photocatalytic Features of an Emulsion -Driven Boron-Doped TiO₂ Nano Powder. *Mol. Catal.* **2018**, *451*, 51–65. [[CrossRef](#)]
4. Dal Santo, V.; Naldoni, A. Titanium Dioxide Photocatalysis. *Catalysts* **2018**, *8*, 591. [[CrossRef](#)]
5. Subramanian, A.; Wang, H.W. Effects of Boron Doping in TiO₂ Nanotubes and the Performance of Dye-Sensitized Solar Cells. *Appl. Surf. Sci.* **2012**, *258*, 6479–6484. [[CrossRef](#)]
6. Dozzi, M.A.; Artiglia, L.; Granozzi, G.; Ohtani, B.; Elena, S. Photocatalytic Activity vs Structural Features of Titanium Dioxide Materials Singly Doped or Co-doped with Fluorine and Boron. *J. Phys. Chem. C* **2004**, *118*, 25579–25589. [[CrossRef](#)]
7. Palmas, D.; Pozzo, A.D.; Mascia, M.; Vacca, A.; Ricci, P.C. Sensitization of TiO₂ Nanostructures with Coumarin 343. *Chem. Eng. J.* **2012**, *211–212*, 285–292. [[CrossRef](#)]
8. Murphy, S.; Saurel, C.; Morrissey, A.; Tobin, J.; Oelgemoller, M.; Nojan, K. Photocatalytic Activity of a Porphyrin/TiO₂ Composite in the Degradation of Pharmaceuticals. *Appl. Catal. B Environ.* **2012**, *119–120*, 156–165. [[CrossRef](#)]
9. Ebrahimian, A.; Zanjanchi, M.A.; Noei, H.; Arvand, M.; Wang, Y. TiO₂ Nanoparticles Containing Sulphonated Cobalt Phthalocyanine: Preparation, Characterization and Photocatalytic Performance. *J. Environ. Chem. Eng.* **2014**, *2*, 484–494. [[CrossRef](#)]
10. Giuseppe, M.; Elisa, G.; Leonardo, P.; Gabriela, D.; Rudolf, S. Photocatalytic Degradation of 4-Nitrophenol in Aqueous Suspension by Using Polycrystalline TiO₂ Impregnated with Lanthanide Double-Decker Phthalocyanine Complexes. *J. Phys. Chem. C.* **2017**, *111*, 6581–6588.
11. Vignesh, K.; Rajarajan, M.; Suganthi, A. Photocatalytic Degradation of Erythromycin under Visible Light by Zinc Phthalocyanine Modified Titania Nanoparticles. *Mater. Sci. Semi. Proc.* **2014**, *23*, 98–103. [[CrossRef](#)]
12. Vargas, E.; Vargas, R.; Nunez, O. A TiO₂ Surface Modified with Copper (II) Phthalocyanine Tetrasulfonic Acid Tetrasodium Salt as a Catalyst During Photoinduced Dichlorvos Mineralization by Visible Solar Light. *Appl. Catal. B Environ.* **2014**, *156–157*, 8–14. [[CrossRef](#)]
13. Albay, C.; Koc, M.; Altin, I.; Bayrak, R.; Degirmencioglu, I. New Dye Sensitized Photocatalysts: Copper (II)-Phthalocyanine/TiO₂ Nanocomposite for Water Remediation. *J. Photochem. Biol. A Chem.* **2016**, *324*, 117–125. [[CrossRef](#)]
14. Szkoda, M.; Lisowska-Oleksiak, A.; Suizdak, K. Optimization of Boron -Doping Process of Titania Nanotubes Via Electrochemical Method Toward Enhanced Photoactivity. *J. Solid State Electrochem.* **2016**, *20*, 1765–1774. [[CrossRef](#)]
15. Wu, Y.; Xing, M.; Zhang, J.; Chen, F. Effective Visible Light-Active Boron and Carbon Modified TiO₂ Photocatalyst for Degradation of Organic Pollutant. *Appl. Catal. B Environ.* **2010**, *97*, 182–189. [[CrossRef](#)]
16. Anucha, C.B.; Altin, I.; Biyiklioglu, Z.; Bacaksiz, E.; Polat, I.; Stathopoulos, V.N. Synthesis, Characterization, and Photocatalytic Evaluation of Manganese (III) Phthalocyanine Sensitized ZnWO₄ (ZnWO₄MnPc) for Bisphenol A Degradation Under UV Irradiation. *Nanomaterials* **2020**, *10*, 2139. [[CrossRef](#)] [[PubMed](#)]
17. Prajapati, S.T.; Gohel, M.C.; Patel, L.D. Studies to Enhance Dissolution Properties of Carbamazepine. *Indian J. Pharm. Sci.* **2007**, *69*, 427–430. [[CrossRef](#)]
18. Ribeiro, R.A.; Nunes, C.O.; Pereira, M.F.R. *Environ Int.* An overview on the Advanced Oxidation Processes Applied for the Treatment of Water Pollutants Defined in the Recently Launched Directive 2013/39/EU. *Environ. Int.* **2015**, *75*, 33–51. [[CrossRef](#)]
19. Doll, T.E.; Frimmel, F.H. Removal of Selected Persistent Organic Pollutants by Heterogeneous Photocatalysis in Water. *Catal. Today* **2005**, *101*, 195–202. [[CrossRef](#)]
20. Miao, X.; Metcalfe, C. Determination of Carbamazepine and its Metabolites in Aqueous Samples using Liquid Chromatography -Electrospray Tandem Mass Spectrometry. *Anal. Chem.* **2003**, *75*, 3731–3738. [[CrossRef](#)]
21. Mugundan, S.; Rajamannan, G.; Viruthagiri, N.; Shanmugam, R.; Gobi, P. Synthesis and Characterization of Undoped and Cobalt-Doped TiO₂ Nanoparticles via Sol-gel Technique. *Appl. Nanosci.* **2015**, *5*, 449–456. [[CrossRef](#)]
22. Altin, I.; Sokmen, M.; Biyiklioglu, Z. Sol gel Synthesis of Cobalt Doped TiO₂ and Its Dye Sensitization for Efficient Pollutant Removal. *Mater. Sci. Semicon. Proc.* **2016**, *45*, 36–44. [[CrossRef](#)]
23. Bayrak, R.; Bekircan, O.; Durmus, M.; Degirmencioglu, I. The Synthesis and Structural Characterization of New Metallo Phthalocyanines with 1,2,4-triazole Fragments. *J. Organomet. Chem.* **2014**, *767*, 101–107. [[CrossRef](#)]

24. Yalcin, I.; Yanik, H.; Akcay, H.T.; Dergimencioglu, I.; Durmus, M. Photophysical and Photochemical Study on the Tetra 4- Isopropylbenzyloxy Substituted Phthalocyanines. *J. Lumin. Source* **2017**, *192*, 739–744. [[CrossRef](#)]
25. Keles, T.; Barut, B.; Ozel, A.; Biyiklioglu, Z. Synthesis of Water-Soluble Silicon Phthalocyanine, Naphthalocyanine Bearing Pyridine Groups and Investigation of their DNA Interaction, Topoisomerase Inhibition, Cytotoxic Effects and Cell Cycle Arrest Properties. *Dyes Pigm.* **2019**, *164*, 372–383. [[CrossRef](#)]
26. Avetta, P.; Prevot, A.B.; Fabbri, D.; Montoneri, E.; Tomasso, L. Photodegradation of Naphthalene Sulphonic Compounds in the Presence of a Bio-Waste Derived Sensitizer. *Chem. J. Eng.* **2012**, *197*, 193–198. [[CrossRef](#)]
27. Manuela, D.; Fabbri, D.; Bianco Prevot, A.; Pramauro, E. Removal of Alkylphenols from Polluted Sites Using Surfactant-Assisted Soil Washing and Photocatalysis. *Environ. Sci. Pollut Res.* **2011**, *18*, 783–789.
28. Carlos, L.; Fabbri, D.; Capparelli, A.L.; Bianco Prevot, A.; Pramauro, E.; Einschlag, F.G. Effect of Simulated Solar Light on the Autocatalytic Degradation of Nitrobenzene Using Fe³⁺ and Hydrogen Peroxide. *J. Photochem. Photobiol. C* **2009**, *201*, 32–38. [[CrossRef](#)]
29. Bas, H.; Biyiklioglu, Z. Non -aggregated Axially Naphthoxacin Group Substituted Silicon Phthalocyanines: Synthesis and Electrochemistry. *J. Organomet. Chem.* **2015**, *791*, 238–243. [[CrossRef](#)]
30. Biyiklioglu, Z. Electrochemical and Aggregation Properties of Newly Synthesized Dendritic Axially Morpholine -Disubstituted Silicon Phthalocyanine, Mono-substituted Sub phthalocyanine and their Quaternized Derivatives. *Inorg. Chem. Commun.* **2015**, *55*, 60–64. [[CrossRef](#)]
31. Demirkapi, D.; Sirin, A.; Yildiz, B.T.; Cakar, Z.P.; Sesalan, B.S. The Synthesis of New Silicon Phthalocyanines and Analysis of their Photochemical and Biological Properties. *Synth. Met.* **2014**, *187*, 152–159. [[CrossRef](#)]
32. Sahin, M.G.; Biyiklioglu, Z.; Durmus, M. The Water Soluble Axially Disubstituted Silicon Phthalocyanines: Photophysicochemical Properties and Invitro Studies. *J. Biol. Inorg. Chem.* **2017**, *22*, 953–967.
33. Bayrak, R.; Akcay, F.S.; Sahin, E.; Bayrak, H.; Dermibas, U. Synthesis, Aggregation and Spectroscopic Studies of Novel Water-Soluble Metal Free Zinc, Copper and Magnesium Phthalocyanines and Investigation of their Anti-Bacterial Properties. *Spectrochim. Acta Part A Mol. Biomol. Spectrosc.* **2014**, *133*, 272–280. [[CrossRef](#)] [[PubMed](#)]
34. Klung, H.P.; Alexander, L.E.; Langford, J.I. X-ray Diffraction Procedures for Polycrystalline and Amorphous Materials. *J. Appl. Crystallogr.* **1975**, *8*, 573–574.
35. Lykaki, M.; Stefa, S.; Carabineiro, S.A.C.; Pandis, K.; Stathopoulos, V.N.; Konsolakis, M. Facet-Dependent Reactivity of Fe₂O₃/CeO₂ Nanocomposites: Effects of Ceria Morphology on CO Oxidation. *Catalysts* **2019**, *9*, 371. [[CrossRef](#)]
36. Stefa, S.; Lykaki, M.; Fragkoulis, D.; Binas, V.; Pandis, P.K.; Stathopoulos, V.N.; Konsolakis, M. Effect of the Preparation Method on the Physicochemical Properties of the CO Oxidation Performance of Nanostructured CeO₂/TiO₂. *Processes* **2020**, *8*, 847. [[CrossRef](#)]
37. Praveen, P.; Viruthagiri, G.; Mugundan, S.; Shanmugam, N. Optical and Morphological Analysis of Pristine Titanium di oxide Nanoparticles via Sol-gel Route. *Spectrochim. Acta Part A Mol. Biomol. Spectrosc.* **2014**, *117*, 622–629. [[CrossRef](#)]
38. Ihara, T.; Miyoshi, M.; Iriyama, Y.; Matsumoto, O.; Sugihara, S. Visible Light Active Titanium Oxide Photocatalyst Realized by an Oxygen -Deficient Structure and by Nitrogen doping. *Appl. Catal. B Environ.* **2003**, *42*, 403–409. [[CrossRef](#)]
39. Herrera-Alonso, M.; Abdala, A.A.; McAllister, M.J.; Aksay, I.A.; Prud'homme, R.K. Intercalation and Stitching of Graphite Oxide with Diamino alkanes. *Langmuir* **2007**, *23*, 10644–10649. [[CrossRef](#)]
40. Zhai, B.G.; Yang, L.; Zhou, F.F.; Shi, J.S.; Huang, Y.M. Strong Photo-Oxidative Capability of ZnWO₄ Nanoplates with Highly Exposed {0 -1 1} Facets. *Catalysts* **2019**, *9*, 178. [[CrossRef](#)]
41. Chen, D.; Yang, D.; Wang, Q.; Jiang, E. Effects of Boron Doping on Photocatalytic Activity and Microstructure of Titanium Dioxide Nanoparticles. *Ind. Eng. Chem. Res.* **2006**, *45*, 4110–4116. [[CrossRef](#)]
42. Li, D.; Xing, Z.; Yu, X.; Cheng, X. One-Step Hydrothermal Synthesis of C-N-S Tri-doped TiO₂ Based Nanosheets Photoelectrode for Enhanced Photo electrocatalytic Performance and Mechanism. *Electrochim. Acta* **2015**, *170*, 182–190. [[CrossRef](#)]
43. Appavoo, I.A.; Hu, J.; Huang, Y.; Li, S.F.Y.; Ong, S.L. Response Surface Modelling of Carbamazepine (CBZ) Removal by Graphene P-25 Nanocomposites/UVA Process using Central Composite Design. *Water Res.* **2014**, *57*, 270–279. [[CrossRef](#)] [[PubMed](#)]

44. Wang, Y.; Huang, Y.; Ho, W.; Zhang, L.; Zhou, Z.; Lee, S. Biomolecule Controlled Hydrothermal Synthesis of C-N-S Tri-doped TiO₂ Nanocrystalline Photocatalyst for NO Removal under Simulated Solar Light Irradiation. *J. Hazard. Mater.* **2009**, *169*, 77–87. [[CrossRef](#)] [[PubMed](#)]
45. Irie, H.; Wantabe, Y.; Hashimoto, K. Nitrogen Concentration Dependence on the Photocatalytic Activity of TiO₂-XN_x Powders. *J. Phys. Chem. B* **2003**, *107*, 5483–5486. [[CrossRef](#)]
46. Silva, C.G.; Faria, J.L. Photocatalytic Oxidation of Phenolic Compounds by Using a Carbon- Nanotube Titanium Dioxide Composite Catalyst. *Chem. SUS Chem.* **2010**, *3*, 609–618. [[CrossRef](#)]
47. Wang, W.; Serp, P.; Kack, P.; Faria, J.L. Photocatalytic Degradation of Phenol on MWNT and Titania Composite Catalyst Prepared by a Modified Sol Gel Method. *Appl. Catal. B.* **2005**, *56*, 305–312. [[CrossRef](#)]
48. Calza, P.; Medana, C.; Padovano, E.; Giacotti, V.; Baiocchi, C. Identification of the Unknown Transformation Products derived from Clarithromycin and Carbamazepine Using Liquid Chromatography/High-Resolution Mass Spectrometry. *Rapid Comm. Mass Spec.* **2012**, 1687–1704. [[CrossRef](#)]
49. Liu, K.; Che-Chin Yu, J.; Dong, H.; Wu, J.C.S.; Hoffmann, M.R. Degradation and Mineralization of Carbamazepine Using an Electro Fenton Reaction Catalysed by Magnetite Nanoparticles Fixed on an Electrocatalytic Carbon Fibre Textile Cathode. *Environ. Sci. Technol.* **2018**, *52*, 12667–12674. [[CrossRef](#)]

Publisher's Note: MDPI stays neutral with regard to jurisdictional claims in published maps and institutional affiliations.



© 2020 by the authors. Licensee MDPI, Basel, Switzerland. This article is an open access article distributed under the terms and conditions of the Creative Commons Attribution (CC BY) license (<http://creativecommons.org/licenses/by/4.0/>).